ELSEVIER

Available online at www.sciencedirect.com
SCIENCE DIRECT®

Journal of Nuclear Materials 355 (2006) 1–9

journal of nuclear materials

www.elsevier.com/locate/jnucmat

Effect of composition on helium diffusion in fluoroapatites investigated with nuclear reaction analysis

S. Miro [a], F. Studer [a], J.-M. Costantini [b,*], J. Haussy [c], P. Trouslard [d], J.-J. Grob [e]

[a] *CRISMAT, ENSICAEN, 6 Bd du Maréchal Juin, F-14050 Caen cedex, France*
[b] *CEA Saclay, DMN/SRMA, F-91191 Gif-sur-Yvette cedex, France*
[c] *CEA DIF, DCRE/SEIM, BP 12, F-91680 Bruyères-le-Châtel cedex, France*
[d] *CEA Saclay, LEMFI/INSTN/DRECAM, F-91191 Gif-sur-Yvette cedex, France*
[e] *CNRS-InESS, 23, rue du Loess, B.P.20, F-67037 Strasbourg cedex, France*

Received 27 September 2005; accepted 4 April 2006

Abstract

In the context of nuclear waste disposal, the knowledge of the diffusion of helium produced by α-decays is an important issue, in order to assess the long-term behavior of the containment matrices. Apatite is one of these potential hosts, which can incorporate many radionuclides as trivalent minor actinides and fission products. In order to determine the influence of the double (cationic/anionic) substitution on helium diffusion, we have studied two different apatite compositions ($Ca_{10}(PO_4)_6F_2$ and $Ca_4Nd_6(SiO_4)_6F_2$). For that purpose, the helium bulk diffusion constants were derived from non-destructive ^{3}He depth profiling using the $^3He(d,p)^4He$ nuclear reaction. Results have been obtained on sintered ceramics implanted with 3-MeV $^3He^+$ ions at a depth around 9 μm with a fluence of 10^{16} ions cm^{-2} then annealed in air at temperatures between 250 and 400 °C. We show that the activation energy for helium diffusion determined by two different models decreases with substitution, i.e., 1.27 eV for $Ca_{10}(PO_4)_6F_2$ and 0.89 eV for $Ca_4Nd_6(SiO_4)_6F_2$. Moreover, the activation energy in sintered $Ca_{10}(PO_4)_6F_2$ ceramics is similar to that determined by other authors on a single crystal of the same composition. It leads us to think that the diffusion mechanism involves the tunnels of the structure, the size of which increases with substitution.

PACS: 66.30; 61.72.S–81.70.J; 24.30.−v

1. Introduction

Apatites are of great interest as waste containment matrices for separated radionuclides. Their structure can indeed incorporate many radionuclides as trivalent minor actinides (Am^{3+}, Cm^{3+}) and fission products (I^-, Cs^+) of ^{235}U. Apatite, in its most common high-symmetry representation [1], is the generic name of a family of calcium phosphates with formula $Me_{10}(XO_4)_6Y_2$ which crystallizes in the hexagonal system $P6_3/m$ (Fig. 1). Me is a divalent cation (Ca^{2+}, Ba^{2+}, etc.) which can be replaced by a monovalent (Na^+, Cs^+, etc.) or

---

[*] Corresponding author. Tel.: +33 1 6908 4388; fax: +33 1 6908 7167.
E-mail address: jean-marc.costantini@cea.fr (J.-M. Costantini).

0022-3115/$ - see front matter © 2006 Elsevier B.V. All rights reserved.
doi:10.1016/j.jnucmat.2006.04.004

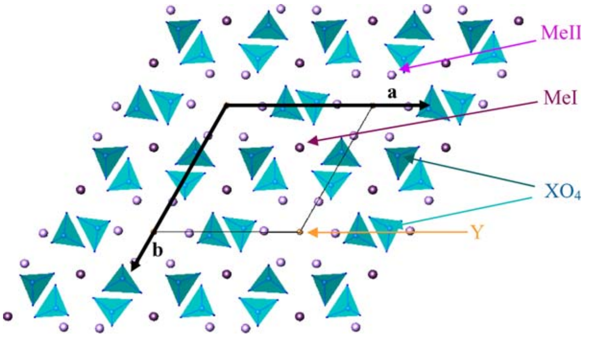

Fig. 1. Projection on the [001] plane of the apatitic structure $Me_{10}(XO_4)_6Y_2$.

trivalent cation (Nd^{3+}, Am^{3+}, Cm^{3+}, etc.), XO_4 a trivalent anion (PO_4^{3-}, VO_4^{3-}, etc.) which can be substituted by a tetravalent (SiO_4^{4-}, GeO_4^{4-}, etc.) or bivalent grouping (SO_4^{2-}, CO_3^{2-}, etc.) and Y a monovalent (F^-, I^-, etc.) and sometimes bivalent anion (O_2^-, CO_3^{2-}, etc.). The quasi-compact arrangement of XO_4 ions constitutes the skeleton of the apatitic structure [2] and reveals two types of tunnels. The first tunnel consists of four cations per cell, noted MeI, located on the 4f sites of the structure and surrounded by nine oxygen atoms. The second tunnel consists of six cations per cell, noted MeII, located on the 6 h sites of the structure and surrounded by six oxygen atoms and one anion Y.

After their production, most of these radionuclides transform following a complex scheme of spontaneous decays characterized in particular by the emission of α particles. For long-term ageing, the helium content in containment matrices could reach large values (>1 at.%) [3]. Since the solution energy of helium in solids is generally large [4], helium atoms will tend to coalesce and form bubbles inducing detrimental modifications of the material's structure and mechanical properties (e.g., embrittlement) [5]. Therefore, it is very important to know how helium diffuses in these matrices.

First studies of helium diffusion in apatites were carried out by Zeitler et al. [6] and Lippolt et al. [7]. These authors, with the aim of dating minerals, by degassing helium have determined activation energies and the relative diffusion coefficients in various apatites coming from different geological media. Zeitler, by studying a Durango fluoroapatite of approximate general formula $Ca_{10}(PO_4)_6F_2$, has determined an activation energy of 1.67 eV. Lippolt, for various compositions of apatite, has given activation energies ranging from 0.73 to 1.97 eV and extrapolated diffusion coefficients at 25 °C ($D^{25\,°C}$) ranging from 10^{-27} to 10^{-17} $cm^2\,s^{-1}$. Another determination was carried out by Ouchani et al. [8] by ERDA (Elastic Recoil Detection Analysis) on a Durango fluoroapatite and two sinters ($Ca_{9.99}Na_{0.01}Nd_{0.01}(PO_4)_6F_2$ and $Ca_{9.80}Na_{0.20}Nd_{0.20}$-$(PO_4)_6F_2$). The thermal diffusion of ^4He was measured in a temperature range 120–250 °C with activation energy of 1.25 ± 0.02 eV and $D^{25\,°C}$ of 10^{-23} $cm^2\,s^{-1}$ for the three samples. These results are in agreement with those of Zeitler and Lippolt. Lastly, by using the $^3He(d,p)^4He$ nuclear reaction on monosilicated sinter ($Ca_9Nd(PO_4)_5(SiO_4)F_2$), Costantini et al. [9] have also studied the ^3He thermal diffusion process on a temperature range 200–400 °C with an activation energy of 1.08 eV and $D^{25\,°C}$ of 5.10^{-23} $cm^2\,s^{-1}$.

Although these studies seem numerous, no study took into account the influence of the double (cationic/anionic) substitution on the helium thermal diffusion process. We have thus studied the thermally-activated migration of ^3He atoms in various fluoroapatites using the $^3He(d,p)^4He$ nuclear reaction, where ^3He acts as a tracer for ^4He diffusion with an isotopic mass factor correction. Although the depth resolution and sensitivity of this technique are known to be low [10–12], diffusion constants can be so-obtained from ^3He depth profiling. We show that helium diffusion depends on the silicate/phosphate substitution.

2. Experiments

We studied two fluoroapatites sintered ceramics: i.e., one fully phosphated $Ca_{10}(PO_4)_6F_2$ and one fully silicated $Ca_4Nd_6(SiO_4)_6F_2$. These ceramics were synthesized by reactive sintering of precursors CaF_2, CaO, $Ca_2P_2O_7$, Nd_2O_3 and SiO_4 in stoechiometric amounts. After being crushed, precursors were compacted in a pellet (diameter of 11 mm and thickness of 1 mm) by pressing at 200 MPa. A heat treatment was thus applied at 1500 °C during 6 h under nitrogen flow [13]. Ceramics were then polished with five discs covered with silicon carbide of granulometry varying from 26 to 5 μm, then with four diamond discs of granulometry varying from 3 to 0.1 μm. They were then heated again at 500 °C during 6 h, as mentioned in Ref. [14]. This thermal annealing induces stress relaxation of the layers, perturbed by polishing, and desorption of the surface atomic layers. Sintered ceramics were characterized by various techniques to check the absence of impurities: EDS (energy dispersive spectrometry), SEM (scanning electron microscopy) and XRD (X-ray diffraction). SEM enabled us to observe a mean grain size of about 20 μm. These grains are acicular crystals for the $Ca_{10}(PO_4)_6F_2$ composition. On the other hand, the $Ca_4Nd_6(SiO_4)_6F_2$ composition does not present any more acicular crystals and the pores density decreases. These observations result from partial fusion of crystals, the melting temperature decreasing with the double (cationic/anionic) substitution. Moreover, XRD allowed us to determine the cell parameters ($a = 9.38(1)$ Å, $c = 6.89(1)$ Å for $Ca_{10}(PO_4)_6F_2$ and $a = 9.53(1)$ Å, $c = 7.01(1)$ Å for $Ca_4Nd_6(SiO_4)_6F_2$) and the theoretical density (3.195(3) g cm^{-3} for $Ca_{10}(PO_4)_6F_2$ and 4.869(3)g cm^{-3} for $Ca_4Nd_6(SiO_4)_6F_2$). Helium pycnometry yielded the skeletal density (2.838(9) g cm^{-3} for $Ca_{10}(PO_4)_6F_2$ and 4.728(9) g cm^{-3} for $Ca_4Nd_6(SiO_4)_6F_2$). The deduced porosity values are 11.2(4)% for $Ca_{10}(PO_4)_6F_2$ and 2.9(3)% for $Ca_4Nd_6(SiO_4)_6F_2$. This difference is in agreement with the SEM observations showing a denser compound in the case of $Ca_4Nd_6(SiO_4)_6F_2$ than in the case of $Ca_{10}(PO_4)_6F_2$, and thus a more significant partial fusion during the heat treatment.

Samples were implanted with 3-MeV ^3He ions at a fluence of 10^{16} cm^{-2} by using the Van de Graaff accelerator of the InESS laboratory (Strasbourg). The projected range and longitudinal straggling of ^3He calculated using SRIM2000 code [15] are, respectively, $R_p = 10.40$ μm and $\Delta R_p = 0.23$ μm in $Ca_{10}(PO_4)_6F_2$, $R_p = 8.62$ μm and $\Delta R_p = 0.30$ μm in $Ca_4Nd_6(SiO_4)_6F_2$. The SRIM He maximum concentration values at this fluence is 1.85×10^{20} cm^{-3} for the $Ca_{10}(PO_4)_6F_2$ composition and 1.40×10^{20} cm^{-3} for the $Ca_4Nd_6(SiO_4)_6F_2$ composition. The SRIM maximum displacements per atom value at this fluence is 0.012 for the $Ca_{10}(PO_4)_6F_2$ composition and 0.016 for the $Ca_4Nd_6(SiO_4)_6F_2$ composition. Samples were then annealed, with positive and negative slopes of about 100 °C min^{-1}, at three different temperatures during various times: 250 °C during 48 h, 325 °C during 1 h and 400 °C during 1 h as performed in Ref. [9].

The ^3He depth profiles were determined by the $^3He(d,p)^4He$ nuclear reaction with the milli-probe of the Van De Graaff accelerator of the INSTN (CEA/Saclay) with a beam diameter of 0.5 mm, an incidence angle of 0° and detection angle of 90 °. The detector solid angle is 2.35 msr and its energy resolution 17 keV. The detector is masked by a 29 μm mylar foil to stop the backscattered deuterons. To minimize charge effects, a thin (10 nm) gold layer is deposited on the sample analyzed surface.

The $^3He(d,p)^4He$ reaction exhibits a maximum cross-section value at 430 keV and a full width at half maximum of 350 keV [9]. This broad cross-section is not adequate to obtain good depth resolution on the ^3He depth profile. At the primary energy of 1.8 MeV, we calculate by using the PYROLE code the energy of protons created at the depth x, the energy of outgoing protons emitted in the acceptance angle of the detector and the detected energy after their transmission through the mylar filter (Fig. 2). As function of depth x, these simple calculations show that the detected energy is almost constant as function as depth. At different primary energies, this conclusion remains unchanged. In our analysis conditions, the ^3He depth profile cannot be measured by the energy spectrometry of the emitted protons. Our solution is to sweep the deuteron beam energy gradually from 1.6 to 0.8 MeV, by steps of 0.2–0.05 MeV. Each step required an acquisition time of 15 min to obtain a spectrum with sufficient good statistics. This energy scan shifts the maximum of the cross section inside the material. For each deuteron energy, the proton yield is plotted on an excitation curve versus deuteron energy (Fig. 3(a) and (b)) which is the convolution of the ^3He depth profile with the cross section. Thus, helium depth profiles can be extracted from the excitation curves of the as-implanted and annealed samples.

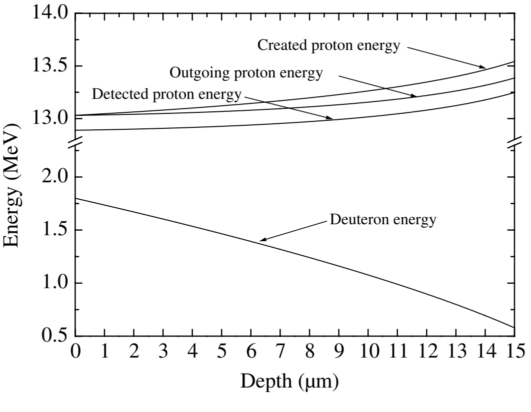

Fig. 2. Particle energies versus ^3He depth in $Ca_{10}(PO_4)_6F_2$ fluoroapatite calculated by Pyrole code [20].

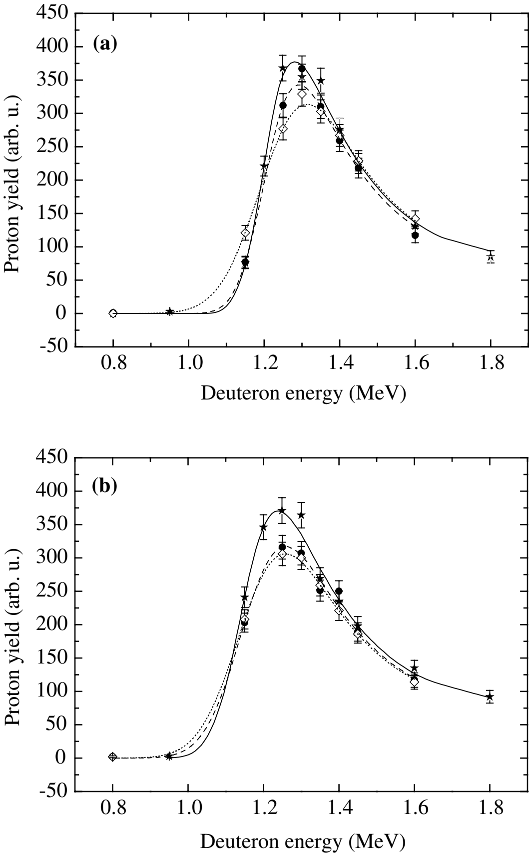

Fig. 3. Experimental and simulated excitation curves of ^{3}He(d,p)^{4}He reaction at various annealing temperatures for $Ca_{10}(PO_4)_6F_2$ (a) and $Ca_4Nd_6(SiO_4)_6F_2$ (b): as-implanted (full stars); 325 °C, 1 h (full circles); 400 °C, 1 h (open diamonds). Lines are least-squares fitted curves to model 1: as-implanted (solid); 325 °C, 1 h (dashed); 400 °C, 1 h (dotted).

3. Data analysis

Excitation curves were analyzed with two different approaches.

3.1. First model

This first model was already used to extract the ^{3}He depth profile in britholite [9]. In this model, the detected proton yield $I_0(E_0)$ at a given incident deuteron energy E_0 is the convolution of the ^{3}He depth profile with the cross section of the nuclear reaction ^{3}He(d,p)^{4}He [16]:

$$I_0(E_0) = \int_0^{x_0} \sigma(E(x))\rho(x)\,\mathrm{d}x, \tag{1}$$

where x_0 is the deuteron projected range, σ, the cross section, $E(x)$, the deuteron energy at depth x (data given by the SRIM 2000 code [15]) and $\rho(x)$, the ^{3}He depth profile. σ depends weakly on the angle of emission θ (for high angular values) at one given energy [17], so that it is possible to neglect the angular dependence in Eq. (1).

To extract the depth profile, it was assumed that the as-implanted ^{3}He profile is Gaussian. This assumption is frequently used in the case of implantation profiles where the third-order ('skewness') and fourth-order ('kurtosis') moments of the distribution are neglected [18]:

$$\rho(x) = A\exp\left[-(x - x_c)^2/2s^2\right] \tag{2}$$

with

$$\int_0^{+\infty} \rho(x)\,\mathrm{d}x = As\sqrt{2\pi}, \tag{3}$$

where A is the amplitude, x_c, the distribution centroid, and s, the standard deviation.

The analysis consists in fitting the three parameters (A, x_c and s) defining the Gaussian profile $\rho(x)$ by using a trial-and-error method. This method, integrated in the AGEING computer code, is based on minimization of an error function between the experimental and the calculated curves [9]. This computer code was elaborated in FORTRAN-90, and transcribed in process control PV-WAVE language.

The optimization of the three parameters (A, x_c and s) is carried out by calling the NLINLSQ (Non LINear Least SQuare) function of PV-WAVE with an optimization algorithm of Levenberg–Marquard type. Options and key words of this function permit to define the initial values of the variables to be optimized, limiting values on these variables (i.e., minimal and maximum values), and several criteria of calculation end (a maximum number of iterations, relative or absolute tolerances). After each optimization, the simulated curve (Fig. 3(a) and (b)) is graphically compared with the experimental points. The error bars on these experimental points are given by $\sqrt{I_0}$ (Fig. 3(a) and (b)). The quality of the fitted parameters is estimated by an error term (Err), which represents the normalized relative error per point between experimental and simulated data:

$$Err = \frac{\sum_{n=1}^{N_{\text{points}}} \left|I_0^{\text{exp}}(n) - I_0^{\text{sim}}(n)\right|}{\max(I_0^{\text{exp}}) \times N_{\text{points}}}, \tag{4}$$

where N_{points} is the number of measurements, I_0^{exp} the experimental and I_0^{sim} the simulated data points. The NLINLSQ function allows to minimize the error function, in order to obtain the three optimal parameters (A, x_c and s), and plot the ^{3}He depth profile (shown for $Ca_{10}(PO_4)_6F_2$ in Fig. 4(a)).

Another program functionality allows us one to study the error function near the found solution. It is particularly useful to visualize the error surface around the optimum given by the NLINLSQ function, this error surface comprising several local minima due to the experimental errors. It consists in evaluating the error term *Err* at different points of a 3D squaring (A, x_c and s) centered on the optimized values. This functionality will be called 'surface'. A good agreement is found between the results given by the two functionalities. The 'surface' functionality yields results characterized by a lower error per point (*Err*). Only the results obtained with this functionality are presented in Tables 1 and 2.

To determine the thermal diffusion coefficients relative to each composition, we have assumed that diffusion follows second Fick's law [19]:

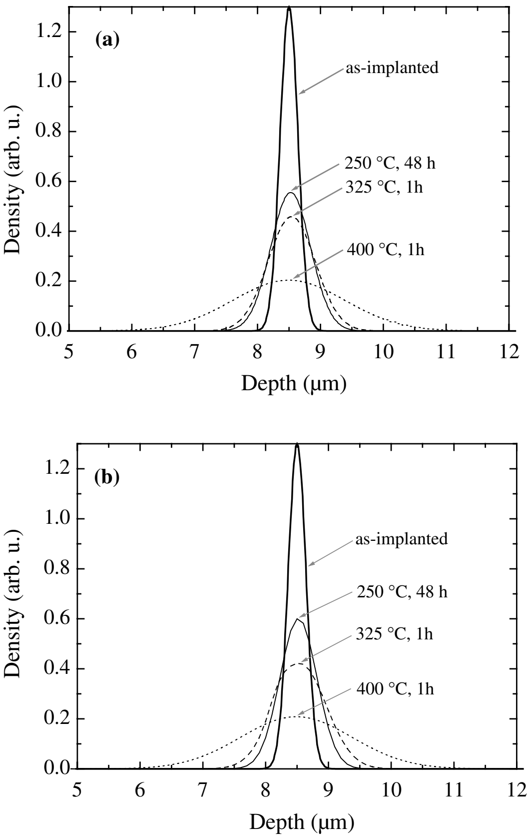

Fig. 4. Gaussian ^{3}He depth profiles in as-implanted and annealed $Ca_{10}(PO_4)_6F_2$, obtained with model 1 (a) and model 2 (b) (see optimized parameters in Table 1).

$$\frac{\partial \rho(x,t)}{\partial t} = D(T)\frac{\partial^2 \rho(x,t)}{\partial x^2}. \tag{5}$$

The diffusion coefficient (D) for a given temperature (T) is then deduced from the relation [19]:

$$D = (s^2 - s_0^2)/(2t), \tag{6}$$

where s is the standard deviation after annealing, s_0, the standard deviation of the as-implanted samples, and t, the annealing time. Such an assumption corresponds to a diffusion process inducing a broadening of the as-implanted Gaussian distribution far from surface sinks (infinite medium conditions) [19].

Diffusion coefficients (D) and optimized parameters (A, x_c and s) obtained for both compositions ($Ca_{10}(PO_4)_6F_2$ and $Ca_4Nd_6(SiO_4)_6F_2$), are displayed in Tables 1 and 2. To estimate the maximum relative error on the optimized parameters, we fitted both experimental excitation curves with $I_0 + \Delta I_0$ and $I_0 - \Delta I_0$, with $\Delta I_0 = \sqrt{I_0}$. The maximum relative errors as well as the maximum relative variations of parameters for both compositions are displayed in Table 3. It is clearly seen that A decreases, s increases and thus D increases versus annealing temperature. By contrast, the integral of the profile, which is proportional to As (Eq. (3)), and x_c do not vary within experimental errors. In spite of an important relative error in the estimation of s parameter, the ^{3}He peak broadening is sufficiently large to determine significant diffusion coefficient values.

Moreover, diffusion processes classically follow an Arrhenius law:

$$D = D^0 \exp\left(-\Delta E/(k_B T)\right), \tag{7}$$

where ΔE is the activation energy of the diffusion process, D^0, the pre-exponential factor, k_B, the Boltzmann constant and T, the annealing temperature. D^0 and ΔE are deduced from the plots of Log D versus $1/T$ (Fig. 5 and Table 4). The maximum relative error on ΔE deduced from this Arrhenius plot is estimated to 4%.

This gives an extrapolated value of $D^{25\,^\circ C}$ for the two compositions (Table 4). Our results are compared with those obtained by ERDA on a Durango fluoroapatite single crystal [8] and those obtained by NRA on a sintered monosilicated sample of chemical formula $Ca_9Nd(PO_4)_5(SiO_4)F_2$ [9] (Fig. 5 and Table 4). In order to compare our results obtained on ^{3}He diffusion with those obtained on ^{4}He diffusion [8], we multiplied the ^{3}He diffusion coefficients by an isotope mass factor of $\sqrt{\frac{4}{3}}$ [19]. The activation energy is the same for a Durango fluoroapatite

Table 1
^{3}He diffusion parameters for the $Ca_{10}(PO_4)_6F_2$ composition at annealing temperature *T* and annealing time *t*

$Ca_{10}(PO_4)_6F_2$			Model 1						Model 2								
T (°C)	*t* (h)	Data	*Err* (%)	*A* (arb. u.)	x_c (μm)	*s* (μm)	*As* (arb. u.)	*D* ($cm^2\ s^{-1}$)	D_1 ($cm^2\ s^{-1}$)	*v* ($\mu m\ h^{-1}$)	*F* (%)	*Err* (%)	*A* (arb. u.)	x_c (μm)	*s* (μm)	*As* (arb. u.)	χ^2
As-implanted		$I_0 - \sqrt{I_0}$	2.03	1.77	8.51	0.97×10^{-1}	1.72×10^{-1}	–	–	–	–	–	–	–	–	–	–
		I_0	1.83	1.30	8.50	1.41×10^{-1}	1.83×10^{-1}										
		$I_0 + \sqrt{I_0}$	1.64	0.99	8.49	1.97×10^{-1}	1.95×10^{-1}										
250	48	$I_0 - \sqrt{I_0}$	2.33	6.98×10^{-1}	8.54	2.69×10^{-1}	1.65×10^{-1}	1.52×10^{-15}	2.12×10^{-15}	-5.48×10^{-4}	4	2.23	6.02×10^{-1}	8.52	2.95×10^{-1}	1.77×10^{-1}	6.17×10^{-11}
		I_0	2.05	5.56×10^{-1}	8.53	3.16×10^{-1}	1.76×10^{-1}	2.31×10^{-15}									
		$I_0 + \sqrt{I_0}$	2.01	5.75×10^{-1}	8.52	3.24×10^{-1}	1.86×10^{-1}	2.46×10^{-15}									
325	1	$I_0 - \sqrt{I_0}$	1.81	5.59×10^{-1}	8.53	2.91×10^{-1}	1.63×10^{-1}	0.90×10^{-13}	2.09×10^{-13}	-5.51×10^{-2}	1	2.85	4.35×10^{-1}	8.53	4.17×10^{-1}	1.81×10^{-1}	1.20×10^{-5}
		I_0	1.52	4.58×10^{-1}	8.54	3.77×10^{-1}	1.73×10^{-1}	1.70×10^{-13}									
		$I_0 + \sqrt{I_0}$	1.45	4.58×10^{-1}	8.53	3.99×10^{-1}	1.83×10^{-1}	1.94×10^{-13}									
400	1	$I_0 - \sqrt{I_0}$	0.86	1.99×10^{-1}	8.50	8.45×10^{-1}	1.68×10^{-1}	0.96×10^{-12}	1.06×10^{-12}	0	0	1.71	2.09×10^{-1}	8.49	8.76×10^{-1}	1.83×10^{-1}	1.46×10^{-10}
		I_0	1.02	2.04×10^{-1}	8.45	8.87×10^{-1}	1.81×10^{-1}	1.07×10^{-12}									
		$I_0 + \sqrt{I_0}$	1.06	2.12×10^{-1}	8.45	9.07×10^{-1}	1.92×10^{-1}	1.11×10^{-12}									

Model 1: Gaussian ^{3}He profile parameters (*A*, x_c and *s*) with the corresponding errors (*Err*) given by the AGEING computer code and diffusion coefficients (*D*) deduced from Eq. (6). Model 2: diffusion coefficient (D_1), transport velocity (*v*), leakage coefficient (*F*) with the corresponding errors (*Err*) given by the AGEING2 computer code and parameters (*A*, x_c, *s*) deduced from Gaussian fit with the χ^2 factor.

Table 2
^{3}He diffusion parameters for the $Ca_4Nd_6(SiO_4)_6F_2$ composition at annealing temperature *T* and annealing time *t*

$Ca_4Nd_6(SiO_4)_6F_2$			Model 1						Model 2								
T (°C)	*t* (h)	Data	*Err* (%)	*A* (arb. u.)	x_c (μm)	*s* (μm)	*As* (arb. u.)	*D* ($cm^2\ s^{-1}$)	D_1 ($cm^2\ s^{-1}$)	*v* ($\mu m\ h^{-1}$)	*F* (%)	*Err* (%)	*A* (arb. u.)	x_c (μm)	*s* (μm)	*As* (arb. u.)	χ^2
As-implanted		$I_0 - \sqrt{I_0}$	1.74	5.73×10^{-1}	7.22	3.04×10^{-1}	1.74×10^{-1}	–	–	–	–	–	–	–	–	–	–
		I_0	1.66	4.89×10^{-1}	7.21	3.85×10^{-1}	1.88×10^{-1}										
		$I_0 + \sqrt{I_0}$	1.77	4.90×10^{-1}	7.21	4.12×10^{-1}	2.02×10^{-1}										
250	48	$I_0 - \sqrt{I_0}$	1.65	2.90×10^{-1}	7.11	6.53×10^{-1}	1.92×10^{-1}	8.05×10^{-15}	7.19×10^{-15}	1.797×10^{-3}	1	1.81	2.99×10^{-1}	7.12	6.30×10^{-1}	1.86×10^{-1}	7.19×10^{-15}
		I_0	1.66	2.88×10^{-1}	7.09	6.61×10^{-1}	1.90×10^{-1}	8.35×10^{-15}									
		$I_0 + \sqrt{I_0}$	1.70	2.83×10^{-1}	7.09	7.12×10^{-1}	2.01×10^{-1}	10.38×10^{-15}									
325	1	$I_0 - \sqrt{I_0}$	3.72	2.68×10^{-1}	7.27	6.04×10^{-1}	1.62×10^{-1}	3.01×10^{-13}	3.44×10^{-13}	-5.03×10^{-2}	9	3.67	2.73×10^{-1}	7.26	6.30×10^{-1}	1.71×10^{-1}	3.44×10^{-13}
		I_0	3.51	2.63×10^{-1}	7.26	6.60×10^{-1}	1.74×10^{-1}	3.99×10^{-13}									
		$I + \sqrt{I_0}$	3.52	2.63×10^{-1}	7.25	7.00×10^{-1}	1.84×10^{-1}	4.75×10^{-13}									
400	1	$I_0 - \sqrt{I_0}$	1.95	2.22×10^{-1}	7.23	7.02×10^{-1}	1.56×10^{-1}	4.78×10^{-13}	4.74×10^{-13}	0	9	1.90	2.40×10^{-1}	7.21	7.00×10^{-1}	1.72×10^{-1}	4.74×10^{-13}
		I_0	0.38	2.31×10^{-1}	7.19	7.44×10^{-1}	1.72×10^{-1}	5.63×10^{-13}									
		$I_0 + \sqrt{I_0}$	1.79	2.26×10^{-1}	7.21	7.78×10^{-1}	1.76×10^{-1}	6.35×10^{-13}									

Model 1: Gaussian ^{3}He profile parameters (*A*, x_c and *s*) with the corresponding errors (*Err*) given by the AGEING computer code and diffusion coefficients (*D*) deduced from Eq. (6). Model 2: Diffusion coefficient (D_1), transport velocity (*v*), leakage coefficient (*F*) with the corresponding errors (*Err*) given by the AGEING2 computer code and parameters (*A*, x_c, *s*) deduced from Gaussian fit with the χ^2 factor.

Table 3
Maximum relative errors and maximum relative variations for ^{3}He diffusion parameters, obtained for both compositions $Ca_{10}(PO_4)_6F_2$ and $Ca_4Nd_6(SiO_4)_6F_2$, with model 1

Composition	Max variation $\Delta A/A$ (%)	Max error $\Delta A/A$ (%)	Max variation $\Delta x_c/x_c$ (%)	Max error $\Delta x_c/x_c$ (%)	Max variation $\Delta s/s$ (%)	Max error $\Delta s/s$ (%)	Max variation $\Delta As/As$ (%)	Max error $\Delta As/As$ (%)	Max variation $\Delta D/D$ (%)	Max error $\Delta D/D$ (%)
$Ca_{10}(PO_4)_6F_2$	84	36	1	1	529	40	5	7	46220	47
$Ca_4Nd_6(SiO_4)_6F_2$	53	17	2	1	93	21	9	9	6643	25

crystal of approximate formula $Ca_{10}(PO_4)_6F_2$ and a sintered ceramics of the same chemical composition. Moreover, the activation energy decreases and the diffusion coefficient D increases when the double (cationic/anionic) substitution increases.

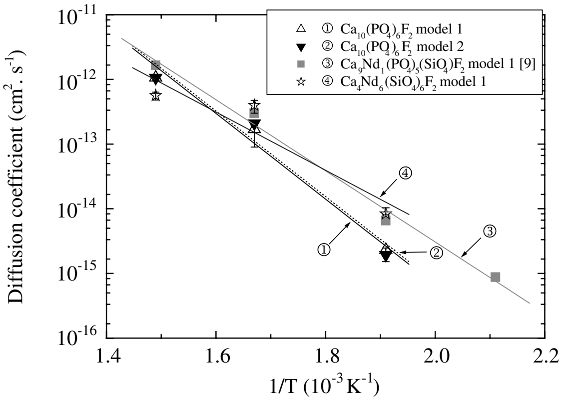

Fig. 5. Arrhenius plot of the ^{3}He diffusion coefficient in $Ca_{10}(PO_4)_6F_2$, $Ca_4Nd_6(SiO_4)_6F_2$ with errors bars (present work) and $Ca_9Nd_1(PO_4)_5(SiO_4)F_2$ [9]. Lines are least-squares linear regressions.

3.2. Second model

In this model, the proton yield $I_0(E_0)$ for an incident deuteron energy E_0 is still written as the convolution of the ^{3}He depth profile with the cross section as in Eq. (1). A Gaussian form was kept for the as-implanted distribution as in Eq. (2). Yet no assumption was made on the annealed ^{3}He depth profile. We also assumed that diffusion follows second Fick's law:

$$\frac{\partial \rho_1(x,t)}{\partial t} = D_1 \frac{\partial^2 \rho_1(x,t)}{\partial x^2} - v\frac{\partial \rho_1(x,t)}{\partial x} - F\rho_1(x,t), \tag{8}$$

where D_1 is the diffusion coefficient, v a phenomenological transport velocity, and F a leakage coefficient of the distribution [19]. $F\rho_1$ corresponds to the helium loss to the surface considered as a

Table 4
Activation energy (ΔE), pre-exponential factor ($D°$) and extrapolated diffusion coefficient at 25 °C ($D^{25\,°C}$) for both compositions $Ca_{10}(PO_4)_6F_2$ and $Ca_4Nd_6(SiO_4)_6F_2$, obtained with model 1 and model 2, compared with data on a natural Durango fluoroapatite [8] and a sintered $Ca_9Nd(PO_4)_5(SiO_4)F_2$ ceramics, obtained with model 1 [9]

Composition	Model	Data	ΔE (eV)	^{4}He diffusion	
				D^0 (cm^2 s^{-1})	$D^{25\,°C}$ (cm^2 s^{-1})
Single crystal $Ca_{10}(PO_4)_6F_2$ [8]	–	–	1.25	1.4×10^{-2}	0.87×10^{-23}
Polycrystal $Ca_{10}(PO_4)_6F_2$	1	$I_0 - \sqrt{I_0}$	1.32	12.30×10^{-3}	
		I_0	1.27	6.1×10^{-3}	0.29×10^{-23}
		$I_0 + \sqrt{I_0}$	1.27	6.25×10^{-3}	
	2	I_0	1.29	9.7×10^{-3}	0.14×10^{-23}
Polycrystal $Ca_9Nd_1(PO_4)_5(SiO_4)F_2$ [9]	1	I_0	1.08	3.0×10^{-4}	17.3×10^{-23}
Polycrystal $Ca_4Nd_6(SiO_4)_6F_2$	1	$I_0 - \sqrt{I_0}$	0.86	2.71×10^{-6}	
		I_0	0.89	5.8×10^{-6}	486×10^{-23}
		$I_0 + \sqrt{I_0}$	0.87	4.57×10^{-6}	
	2	I_0	0.89	4.5×10^{-6}	380×10^{-23}

Our results on ^{3}He diffusion were multiplied by a isotopic factor of $\sqrt{\frac{4}{3}}$ to obtain data for ^{4}He and compare them with those of Ouchani et al. [8].

diffusion sink. These three parameters were optimized by using a trial-and-error method, based on minimization of an error function (*Err*), as in Eq. (4), with the limiting conditions $\rho_1(0,t) = 0$ and $\frac{\partial \rho_1(0,t)}{\partial x} = 0$, $\forall t$, expressing that helium cannot accumulate at the surface.

This new model was integrated in the AGEING2 computer code in PV-WAVE programming language. Calling the NLINLSQ function allows to optimize the D_1, v and F parameters. However, the functionality solving local minima of error surfaces was not implemented as yet.

The results obtained on thermally-annealed $Ca_{10}(PO_4)_6F_2$ and $Ca_4Nd_6(SiO_4)_6F_2$ samples with this program are compared to the former results obtained with AGEING computer code. AGEING2 computer code will then directly give the D_1, v and F values for each annealing (Tables 1 and 2), with the same initial conditions as previously.

The optimized depth profiles of annealed samples are shown for $Ca_{10}(PO_4)_6F_2$ in Fig. 4(b). To compare both models, these depth profiles were least squares fitted with a Gaussian distribution. The corresponding parameters (A, x_c and s) are given in Tables 1 and 2 for both compositions.

It is to be noted that the transport velocity is practically null and independent of composition ($\max|v| = 5.51 \times 10^{-2}$ μm h^{-1} for $Ca_{10}(PO_4)_6F_2$ and 5.03×10^{-2} μm h^{-1} for $Ca_4Nd_6(SiO_4)_6F_2$), in agreement with the fact that x_c does not vary in model 1. The low leakage term (F) values ($\max|F| = 4\%$ for $Ca_{10}(PO_4)_6F_2$ and 9% for $Ca_4Nd_6(SiO_4)_6F_2$) are in agreement with the invariability of the As parameter defined in model 1. The helium loss to the surface seems to be negligible. The D_1 diffusion coefficient values are comparable to results given by the first model within experimental errors. D_1 increases with the annealing temperature according to Eq. (7) which also yields D^0, $D^{25\,°C}$ and ΔE values in good agreement with model 1 (Fig. 5 and Table 4). This allows us to deal with the thermal diffusion process without going through the determination of ^{3}He depth profiles. However, only the first model permits to determine the initial as-implanted profile.

4. Discussion

These results enable us to discuss on the validity of the models and on the activation energy and diffusion coefficient values. Excellent agreement is found with Gaussian profiles in model 2 (χ^2 in Tables 1 and 2). The assumption of the conservation of a Gaussian profile after diffusion, taken in the first model is thus completely justified within sight of the results given by the second model. Moreover, it is seen that optimized parameters (A, x_c and s) values given by both models are equivalent (Tables 1 and 2). Therefore, the two models can be used indifferently to determine the diffusion coefficients and activation energies.

We observe that the activation energies determined in all compositions are low (around 1 eV). Furthermore, the activation energy determined on $Ca_{10}(PO_4)_6F_2$ sintered ceramics and on the Durango fluoroapatite single crystal with the same composition $Ca_{10}(PO_4)_6F_2$ [8], are practically equivalent in regard of experimental error (4%). This confirms conclusions on $Ca_9Nd_1(PO_4)_5(SiO_4)F_2$ [9] ruling out a diffusion mechanism involving grain boundaries or pores of the ceramics. At last, the activation energy decreases and the diffusion coefficient increases with the double (cationic/anionic) substitution. The activation energy difference between both compositions is about 30%, i.e., much larger than the maximum estimated relative error. This evolution is consistent with previous measurements on $Ca_9Nd_1(PO_4)_5(SiO_4)F_2$ [9] yielding $\Delta E = 1.08$ eV. It means that ΔE decreases versus the silicate/phosphate content.

Three different mechanisms of helium diffusion in solids are known to occur: the interstitial, substitutional and dissociative ones [4,5]. In metals, it is fairly well established that the interstitial mechanism occurs only at low temperatures (<100 K) with small migration enthalpies (e.g., <0.5 eV in b.c.c. transition metals) [4]: as temperature rises helium atoms are rapidly trapped by the native or irradiation-induced vacancies since the solution energy is large ($\geqslant 3$ eV) [4,5]. Helium diffusion at high temperatures or under displacive irradiation proceeds either through a substitutional mechanism involving the vacancy-assisted migration or the dissociative mechanism involving helium–vacancy (V) clusters (He_n–V_m) in which helium atoms are trapped [12]. These clusters can act as nucleation centers of gas bubbles at large concentrations. For the substitutional mechanism, the migration activation energy is above 3–4 eV [4]. It is to be noted that the latter process requires a large vacancy concentration in order to take place. For the dissociative mechanism, the activation energies raise to about 4–5 eV in metals [4,5].

In oxides, very few data are available in the literature and mostly for close-packed cubic structures. For instance in MgO, theoretical calculations of the binding energies of a He atom in clusters yield activation energies for the dissociative mechanism of 3.9 eV for one vacancy (He–V) and 3.6 eV for He_n–V_m clusters [21]. For the interstitial and substitutional mechanisms, it would, respectively, yield values of 0.71 and 5.4 eV [21].

In the case of apatites, we think that the activation energy about 1 eV could correspond to a helium diffusion mechanism through the tunnels of the apatitic structure, as previously suggested for the monosilicated britholite [9]. Through the results obtained on the $Ca_4Nd_6(SiO_4)_6F_2$ material, the ^{3}He diffusion enhancement can be attributed to the double (cationic/anionic) substitution and related to the increasing after substitution of the cell parameters values ($a = 9.38(1)$, $c = 6.89(1)$ for $Ca_{10}(PO_4)_6F_2$, $a = 9.41(1)$, $c = 6.91(1)$ for $Ca_9Nd(PO_4)_5(SiO_4)F_2$ and $a = 9.53$, $c = 7.01$ for $Ca_4Nd_6(SiO_4)_6F_2$) and then of the size of the tunnels.

5. Conclusions

We have determined the helium diffusion constants in two different apatite compositions ($Ca_{10}(PO_4)_6F_2$ and $Ca_4Nd_6(SiO_4)_6F_2$), to determine the influence of the substitution (cationic/anionic) on helium diffusion. This study was performed between 200 and 400 °C by a non-destructive ^{3}He depth profiling using the $^3He(d,p)^4He$ nuclear reaction. For this purpose, 3-MeV $^3He^+$ ions were implanted at a depth around 9 μm with a fluence of 10^{16} ions cm^{-2}. The emission yield of 13-MeV protons was measured versus the deuteron incident energy for as-implanted and annealed samples. By fitting calculated excitation curves to the experimental data with two different models: model 1 with a Gaussian assumption on the annealed ^{3}He depth profile, and model 2 with no assumption on the annealed ^{3}He depth profile. The ^{3}He depth profile parameters were deduced before and after annealing at various temperatures.

Diffusion constants are then derived from depth profile broadening. Arrhenius plots of these data yield activation energies of 1.27 eV (model 1) and 1.29 eV (model 2) for $Ca_{10}(PO_4)_6F_2$ and of 0.89 eV (with both models) for $Ca_4Nd_6(SiO_4)_6F_2$. Moreover, the activation energy determined in sintered samples is the same as that determined on the Durango fluoroapatite single crystal with the same composition.

We conclude that the Gaussian assumption of model 1 is completely justified due to the good agreement between both models. In addition, the activation energy is the same in a single crystal and a polycrystalline sample with the same composition, and decreases with substitution, i.e., when the tunnel size increases. These results lead us to think that the diffusion mechanism involves the tunnels of the apatitic structure. The large helium diffusion constant increasing with the double (cationic/anionic) substitution is an asset for the use of apatites as nuclear waste containment matrices.

References

[1] C. Rey, L'actualité Chim. (1995) 41.
[2] J.C. Elliot, London University Thesis, 1964.
[3] W.J. Weber et al., J. Mater. Res. 13 (1998) 1434.
[4] D.J. Reed, Radiat. Eff. 31 (1977) 129.
[5] S.E. Donnelly, J.H. Evans (Eds.), Fundamentals of Inert Gases in Solids, Plenum, New York, 1991.
[6] P.K. Zeitler, A.L. Herczeg, I. McDougall, M. Honda, Geochim. Cosmochim. Acta 51 (1987) 2865.
[7] H.J. Lippolt, M. Leitz, R.S. Wernicke, B. Hagedorn, Chem. Geol. Isotope 112 (1994) 179.
[8] S. Ouchani, J.C. Dran, J. Chaumont, Appl. Geochem. 13 (1998) 707.
[9] J-M. Costantini, P. Trocelier, J. Haussy, J.-J. Grob, Nucl. Instrum. and Meth. B 195 (2002) 400.
[10] F. Paszti, Nucl. Instrum. and Meth. B 66 (1992) 83.
[11] P.P. Pronko, J.G. Pronko, Phys. Rev. B 9 (1974) 2870.
[12] M.B. Lewis, K. Farell, Nucl. Instrum. and Meth. B 16 (1986) 163.
[13] L. Boyer, Toulouse University Thesis, 1998.
[14] F. Villa, Franche-Comté University Thesis, 1997.
[15] J.P. Biersack, L.G. Haggmark, Nucl. Instrum. and Meth. 174 (1980) 257.
[16] M.B. Lewis, N.H. Packan, G.F. Wells, R.A. Buhl, Nucl. Instrum. and Meth. 167 (1979) 233.
[17] J.R. Tesmer, M. Nastasi (Eds.), Handbook of Modern Ion-Beam Materials Analysis, MRS, Pittsburgh, 1995, p. 159.
[18] M. Nastasi, J.W. Mayer, J.K. Hirvonen, Ion–Solid Interactions. Fundamentals and Applications, Cambridge University, New York, 1996.
[19] J. Philibert, 'Diffusion et transport de matière dans les solides', Ed. de Physique, Paris, 1985.
[20] P. Trouslard, PYROLE, CEA-R-5703, 1995.
[21] G. Busker, M.A. Van Huis, R.W. Grimes, A. Van Veen, Nucl. Instrum. and Meth. B 171 (2000) 528.